Nanoscale

M13 bacteriophage spheroids as scaffolds for directed synthesis of spiky gold nanostructures

Journal:	*Nanoscale*
Manuscript ID	NR-ART-04-2018-003229.R1
Article Type:	Paper
Date Submitted by the Author:	06-Jun-2018
Complete List of Authors:	Ngo-Duc, Tam-Triet; University of California, Riverside, Materials Science and Engineering Program Plank, Joshua; University of California, Riverside, Electrical and Computer Engineering Chen, Gongde; University of California, Riverside, Chemical and Environmental Engineering Harrison, Reed; University of California Riverside, Bioengineering Morikis, Dimitrios; University of California, Riverside, Bioengineering Liu, Haizhou; University of California, Riverside, Chemical and Environmental Engineering Haberer, Elaine; University of California, Riverside, Department of Electrical and Computer Engineering; University of California, Riverside, Materials Science and Engineering Program

M13 bacteriophage spheroids as scaffolds for directed synthesis of spiky gold nanostructures

Tam-Triet Ngo-Duc[1], Joshua M. Plank[2], Gongde Chen[3], Reed E. S. Harrison[4], Dimitrios Morikis[4], Haizhou Liu[3], Elaine D. Haberer [1,2]

[1]*Materials Science and Engineering Program, University of California, Riverside*
[2]*Department of Electrical and Computer Engineering, University of California, Riverside*
[3]*Department of Chemical and Environmental Engineering, University of California, Riverside*
[4]*Department of Bioengineering, University of California, Riverside*

ABSTRACT

The spherical form (s-form) of a genetically-modified gold-binding M13 bacteriophage was investigated as a scaffold for gold synthesis. Repeated mixing of the phage with chloroform caused a 15-fold contraction from a nearly one micron long filament to an approximately 60 nm diameter spheroid. The geometry of the viral template and the helicity of its major coat protein were monitored throughout the transformation process using electron microscopy and circular dichroism spectroscopy, respectively. The transformed virus, which retained both its gold-binding and mineralization properties, was used to assemble gold colloid clusters and synthesize gold nanostructures. Spheroid-templated gold synthesis products differed in morphology from filament-templated ones. Spike-like structures protruded from the spherical template while isotropic particles developed on the filamentous template. Using inductively coupled plasma-mass spectroscopy (ICP-MS), gold ion adsorption was found to be comparatively high for the gold-binding M13 spheroid, and likely contributed to the dissimilar gold morphology. Template contraction was believed to modify the density, as well as the avidity of gold-binding peptides on the scaffold surface. The use of the s-form of the M13 bacteriophage significantly expands the templating capabilities of this viral platform and introduces the potential for further morphological control of a variety of inorganic material systems.

1. Introduction

The fast pace of nanotechnology development has boosted demand for versatile manufacturing techniques capable of arranging molecular and nanoscale objects with nanometer precision. For millennia, nature has been assembling complex, highly-organized nanostructures. Among these are viral capsids. These robust, monodisperse, bio-based nanoparticles are exceptional scaffolds

for nanomaterial assembly. Viruses exist in a multitude of shapes and sizes from icosahedrons to high-aspect-ratio filaments and from tens to hundreds of nanometers in dimension, thus providing an array of template geometries.[1,2] Moreover, binding sites for specific materials, often referred to as fusion peptides, can be integrated into viral structural proteins. The locations, quantities, and functionalities of fusion peptides are encoded within the viral genetic material, making templates highly programmable.[1] Equally as important for nanomanufacturing, the mass production of viruses is not only possible, but environmentally-friendly and cost effective.[2] Viral templates have formed a variety of materials and nanoarchitectures[3,4,13,5–12], spanning metal-semiconductor core-shell structures to perovskite nanowires and have found application in battery electrodes[14,15], supercapacitors[16], sensors[17,18], biomedical tools[19,20], photocatalytic materials[3], and photovoltaics.[21]

Yet, a fundamental limitation remains for viral templates: the inability to radically modify geometry. The structure of most viruses is largely constrained, allowing only modest dimensional or volumetric changes. For example, in response to changes in pH or salt concentration, a mere 10% increase in diameter of the cowpea chlorotic mottle virus can be attained and the capsid remains icosahedral.[22] As such, if a substantially different size or shape template is required for a specific application, a virus with corresponding architecture must be selected and appropriately modified with fusion peptides. This lack of adaptability restricts viral template usage. Notably, a few plant viruses have exhibited more substantial shape conversion. When exposed to heat, the tobacco mosaic virus (TMV), is reduced from a 300 nm rod to a 170 nm sphere[23,24], and the potato virus X (PVX) shrinks from a 515 nm rod to a 48 nm sphere.[25] TMV transformation has been exploited for biomedical applications such as bio-compatible nanoparticles[26] and magnetic resonance imaging (MRI) contrast reagents.[27]

A more extreme case of viral shape transformation is displayed by the Ff class of bacteriophage, including f1, fd, and M13. These filamentous, non-lytic viruses have been developed as combinatorial phage display peptide library workhorses, with the pIII and pVIII viral proteins used most frequently for this purpose.[28] Three to five copies of the pIII minor coat protein are located at the proximal or infectious end of the phage. And, a few thousand copies of the pVIII major coat protein run the length of the nearly 1 micron long virus in a right-handed α-helix with five-fold rotational symmetry and a two-fold screw axis.[28] Ff bacteriophage libraries

have been used to discover numerous fusion peptides that selectively bind and template materials of technological consequence.[5,29–33] For example, gold-binding motifs displayed on the M13 and fd bacteriophage have been used to assemble or manufacture a variety of gold morphologies including nanoparticles, nanochains, and nanocubes for devices such as chemiresistive and surface-enhanced Raman scattering (SERS) sensors, as well as biofuel cells.[17,34–39] Contact with a water/chloroform interface can cause Ff viruses to contract from 3- to 20-fold producing rod-shaped intermediate forms (i-forms) 100s of nanometers in length and hollow spheroids (s-forms) 10s of nanometers in diameter, depending on conditions. Although the precise mechanism is unknown[40,41], chloroform is thought to alter the hydrophobic protein-protein interactions of the major coat proteins. As such, pVIII proteins slide relative to one another causing long range conformational changes to the virus.[42–44] This chloroform-triggered transformation was initially studied in the early 1980s in the M13 by Griffith and colleagues and was thought to mimic the *E. coli* host infection process.[40,41] Later, chloroform treatment was used as a tool by Petrenko et al., in conjunction with enzyme-linked immunosorbent assay (ELISA), to study the global binding behavior of fusion peptides or "substitute antibodies" located on the fd phage body.[45] Still, more recently, monolayers of bioreceptors for piezoelectric resonator-based bacteria sensors were created from the major coat proteins of ruptured fd spheroids.[46] Although the filamentous form of the Ff class bacteriophage has been used regularly as a scaffold for nanomaterial assembly, its s-form is completely unexplored for this purpose.

In this study, we examine the chloroform-driven conversion of a M13 bacteriophage with pVIII gold-binding peptide fusions and the impact of this shape change on its material assembly capabilities. The gold affinity of the virus was preserved after transformation from filament to spheroid, such that the assembly of gold colloid and synthesis of gold nanostructures were supported. Interestingly, increased gold ion uptake was observed for spheroids as compared to filaments, despite reduced surface area. Moreover, increased nanoparticle density and a distinct spike-like gold morphology were observed for s-forms. This M13 bacteriophage template transformation scheme is believed to be broadly applicable and can be extended to a range of Ff class bacteriophage and nanostructured materials.

2. Materials and methods

M13 transformation

The transformation of a M13 bacteriophage modified to display a gold-binding peptide sequence, VSGSSPDS[38], at the N-terminus of each pVIII protein was studied. Phage were converted from filamentous to s-form using a chloroform treatment method adapted from previous reports.[40,46] The filamentous gold-binding phage were dispersed in tris-buffered saline (TBS, 50 mM Tris–HCl, 150 mM NaCl, pH 7.5) at a concentration of 10^8 pfu/µl. Equal volumes of phage solution and amylene-stabilized chloroform (99.8%, ACROS Organics) were combined at room temperature to a total volume of 200 µL. The mixture was initially vortexed at high power for 2 s and allowed to stand for 13 s. Subsequently, this process was repeated at low power 1 to 15 times. Following transformation, 90-100 µL of chloroform was removed and air was gently blown over the sample for 15 s to ensure removal of residual chloroform. For comparison, wild-type (unmodified) phage were converted using the same procedure, as well as two other gold-binding filament concentrations (5 x 10^8 pfu/µl and 1 x 10^9 pfu/µl).

Circular dichroism (CD) measurements

In order to study the secondary structure of the major coat protein (pVIII) during the transformation process, spectra of filaments and spheroids were collected using a circular dichroism (CD) spectrometer (JASCO, J-815). Measurements were taken at different stages of transformation from 0 to 16 vortex cycles. These measurements were performed at room temperature in the wavelength range of 205 to 235 nm. The instrument settings were as follows: 50 nm/min scan speed, 1 nm bandwidth, 4 s response time, and 12 scan accumulations. To improve the signal-to-noise ratio, three samples were measured and averaged at each vortex condition.

Gold binding on the M13 phage

The gold-binding functionality of the s-forms was studied with 5 nm colloidal gold solution (5 x 10^{13} particles/mL, BBI Solutions). Equal parts 5 nm diameter gold colloid and 10^8 pfu/µL spheroid solution were combined, briefly vortexed, and allowed to incubate for 10 min prior to transmission electron microscopy (TEM) preparation.

Gold synthesis on the M13 phage

Both filamentous and chloroform-treated gold-binding phage were used as templates for gold synthesis. Chloroauric acid ($HAuCl_4$, Sigma Aldrich) was added to 100 µl of 5 x 10^7 pfu/µL phage solution for a final concentration of 250 µM and incubated at room temperature in the dark for an hour. Subsequently, under constant stirring, 50 µL of sodium borohydride ($NaBH_4$, Sigma Aldrich) was added every 30 s to achieve final $NaBH_4$ concentrations of 4.2 µM, 9.4 µM, 31.3 µM and 62.5 µM. Samples were immediately prepared for TEM and ultraviolet-visible (UV-Vis) absorption spectroscopy measurements. For comparison, chloroform-treated, wild-type phage were also used as templates for gold synthesis.

Transmission electron microscopy (TEM) sample preparation and characterization

A transmission electron microscope (TEM, Tecnai T12) was used to examine the size and shape of the gold-binding phage before and after transformation, as well as to study its gold binding and synthesis capabilities. For this analysis, a 5 µL sample volume was pipetted onto a formvar/carbon-coated copper grid (Ted Pella, Inc.), incubated for 5 min, rinsed twice with deionized water, and wicked dry with filter paper. Prior to drying, samples without gold were stained with uranyl acetate[47]. ImageJ software was used for TEM image processing and analysis. An ellipse was fitted to each spheroid, and major and minor axes lengths were measured and averaged. To separate spheroids from other possible structures such as i-forms and filaments, structures with an aspect ratio > 3 were excluded. A tracing tool was used to accurately select the irregular shape of each templated gold colloid cluster and synthesized gold nanostructure, an ellipse was fitted to the selected structure, and the major and minor axes length were measured and averaged.

Measurement and analysis of gold ion adsorption on the M13 phage

The adsorption of gold ions onto the untransformed and transformed phage was investigated using inductively coupled plasma-mass spectroscopy (ICP-MS, Agilent 7700x). The templates were prepared to a concentration of 10^8 pfu/µL in TBS and $HAuCl_4$ was added to each phage solution at final concentrations ranging from 0 to 500 µM. The solutions were incubated at room temperature in the dark for an hour to ensure sorption equilibrium. A centrifugal filter (Amicon Ultra-0.5, 3 kDa) was used to remove phage and recover the filtrate. Control solutions without phage were also prepared in the same manner. Both filtrate and control solutions were analyzed

using ICP-MS. To determine the uptake of the viral templates, the gold ion concentration of the filtrate solution was subtracted from that of the control solution for each $HAuCl_4$ concentration. The maximum adsorption capacity, q_{max}, and the Langmuir constant, a, were determined by fitting the slope-intercept form of the Langmuir isotherm

$$q_e = \frac{q_{max} a C_e}{1 + a C_e}$$

where q_e is the gold concentration adsorbed on the phage at equilibrium and C_e is the concentration of gold at equilibrium.[48–50]

Ultraviolet-visible (UV-Vis) spectroscopy

Ultraviolet-visible (UV-Vis) absorption spectroscopy (ThermoFisher, Evolution 60) was used to evaluate the phage concentration before and after transformation, as well as the optical properties of the gold nanomaterial synthesized on filamentous and spheroidal templates. Using a quartz cuvette with a 10 mm optical path length, measurements were made from 220 nm to 380 nm and 400 to 900 nm to determine the phage concentration and optical properties, respectively. The concentration of the filamentous and spheroidal templates were quantified via a previously published protocol.[28] Due to significant geometric change associated with transformation, the absorbance spectra of the spheroids were corrected for Rayleigh scattering as described by Porterfield et al.[51] In brief, a two point approximation of wavelength-dependent scattering (λ^{-4}) was estimated at 340 nm and 360 nm where minimal absorbance was expected from viral proteins and nucleic acids.

Molecular modeling of pVIII gold-binding peptide fusion

Template structures of pVIII for modeling were acquired from the Protein Data Bank[52] using identifiers 1ifd[53] and 1mzt[54] for structures before and after chloroform treatment, respectively. Homology models of pVIII with the gold-binding sequence VSGSSPDS added at the N-termini of the template structures were prepared using Modeller.[55] Molecular visualization and analysis were performed using UCSF Chimera.[56]

3. Results and discussion

A cycle-by-cycle investigation of the transformation process for the gold-binding phage using circular dichroism (CD) measurements revealed a progressive decrease in molar ellipticity. CD spectra from the gold-binding phage are shown in Fig. 1. When assembled within the M13 filamentous form, the pVIII protein has an alpha-helix secondary structure.[28,57,58] Upon transformation via interaction with chloroform, the pVIII protein undergoes a structural change which is similar to that experienced during host infection.[40,44] As illustrated in Fig. 2, the pVIII is believed to shift from a single, somewhat curved alpha-helix to an L-shaped structure composed of two distinct alpha-helices connected by a loop region.[59–61] This conformational change has been associated with a reduction of helicity from 90% to about 60%[43], as well as weakened chromophore coupling between tryptophan and phenylalanine residues on neighboring proteins.[62] Because the major coat protein accounts for more than 85% of the mass of the viral capsid[28,63] and 99% of the protein mass[64], these structural changes dictate the CD spectrum and can be readily observed.[65] The signature ellipticity of an alpha-helix structure within the deep UV region, includes negative bands at 222 nm and 208 nm.[61,66–68] As shown in Fig. 1, both 222 nm and 208 nm band intensities of the gold-binding phage decreased when vortexed with chloroform. Specifically, the ellipticity of the 222 nm band steadily decreased from cycle 0 to 6. Beyond cycle 6, the rate of decrease of molar ellipticity per cycle slowed substantially such that very little additional reduction was observed. The initial decrease in 222 nm band ellipticity with cycle number was attributed to the combined effect of diminished helicity and reduced π-stacking interaction between adjacent pVIII molecules. At higher cycle numbers, it is believed that the majority of the pVIII molecules were converted to the L-shaped structure therefore the reduction in the negative 222 nm band plateaued.

Cycle-by-cycle TEM images, shown in Fig. S1, revealed that the structurally affected pVIII proteins detected with CD spectroscopy were not uniformly distributed throughout the chloroform-treated M13 bacteriophage, but rather, heavily concentrated within specific phage. That is, whereas some viruses were completely transformed into spheroids within the initial vortex cycles, other viruses were seemingly entirely unchanged and remained filaments. With increased cycle number, more spheroids were produced until, at high cycle numbers, spheroids became the dominant geometry. In addition, a small, gradual increase in spheroid size was measured with successive vortex cycles (Fig. S2). Although filaments and spheroids were the most prevalent structures found within the chloroform-treated samples, a few large irregularly-

shaped assemblies, on the order of a few hundred nanometers, were also observed, particularly at higher cycle numbers. Such structures may be derived from aggregates of s-forms and/or i-forms created either during chloroform treatment or TEM sample preparation. Although not evident in all reports of chloroform-treated M13 phage[41,46], the presence of agglomerates and i-forms was previously described by Olsen et al.[46].

Based on CD and TEM data, phage transformed using 5 vortex cycles were selected for further investigation. These gold-binding phage displayed sufficiently reduced 222 nm band ellipticity, as well as 100% filament-to-spheroid conversion. In addition, absorbance spectra indicated that the template concentration was essentially retained (99.8%, Fig. S3) post transformation. Fig. 3 shows the morphology of the filamentous and the spheroidal gold-binding phage before (0 vortex cycles) and after chloroform treatment (5 vortex cycles), respectively. Prior to chloroform treatment, the gold-binding phage were filaments 912 ± 14 nm long. This is slightly larger than the unmodified, M13 wild-type phage which is approximately 880 nm long.[64] The length of filamentous phage is determined by the enclosed genome and can range from 50 to 2000 nm or more depending on the scope of the genetic modification.[69–71] As is apparent in Fig. 3 and reinforced by Fig. S4, the significantly contracted gold-binding spheroids had a rounded, slightly deflated characteristic shape. The average size (59 ± 16 nm) and size distribution of the spheroids is shown in Fig. 4. The s-form size was consistent across samples (Fig. S5). For comparison, wild-type M13 phage were transformed using the same procedure and the corresponding spheroid size distribution is shown in Fig. S6. The spheroidal wild-type phage were slightly smaller than the s-forms produced from gold-binding phage (53 ± 9 nm), in addition a significant number of wild-type filaments (~44%) were still present. Discrepancies in spheroid size and conversion efficiency may be associated with differences in interaction among modified (gold-binding) and unmodified (wild-type) pVIII coat proteins within the viral capsid. Further studies are necessary to better understand the role of peptide fusions on template transformation. Initial phage concentration had a small impact on spheroid size (Fig. S7) and conversion efficiency. Increased template concentrations of 5×10^8 pfu/µl and 1×10^9 pfu/µl produced spheroids 61 ± 18 nm in size with ~98% efficiency and spheroids 65 ± 20 nm in size with ~96% efficiency, respectively.

The peptide, VSGSSPDS, has demonstrated affinity for gold when incorporated as a pVIII insert within the filamentous M13 bacteriophage.[38] Yet, because the affinity of displayed peptides can be dependent on peptide-protein interactions along the phage body[45], the binding capabilities of the VSGSSPDS pVIII peptide fusion were examined following chloroform treatment. As such, s-forms were incubated with 5 nm colloidal gold solution. As shown in the low magnification TEM image in Fig. 5(a), following incubation both small groups and larger clusters of colloid were observed. While the smaller groups of nanoparticles were attributed to reduced electrostatic repulsion caused by the introduction of buffer salts with the template, histograms of gold colloid assembly size (Fig. S8) with and without spheroids confirmed the larger clusters (>60 nm) were strictly associated with the presence of the template. Higher magnification TEM images of a spheroidal viral template and a large colloidal nanoparticle cluster are shown in Fig. 5(b) and (c), respectively. The relative size and geometry of the template and cluster further supported the decoration of spheroids with gold nanoparticles. Additionally, samples stained with uranyl acetate (Fig. S9) definitively demonstrated co-location of s-forms and nanoparticle clusters. Repeatability of the formation of gold clusters through binding was demonstrated across samples (Fig. S10). The colloidal nanoparticles were closely-packed and randomly arranged on the surface of the viral template. Because the positions of the gold-binding peptides on the M13 spheroid surface were likely densely packed without long range organization, we believe that a one-to-one peptide-to-nanoparticle binding ratio was prevented and relative disorder promoted. A 24 nm redshift in peak optical absorbance, as shown in Fig. S11, corroborated the close proximity of the bound nanoparticles on the viral templates. Despite the estimated 15-fold one-dimensional contraction and the nearly 1.8-fold surface area reduction associated with spheroid formation, the gold-binding peptide clearly retained an affinity for gold after chloroform treatment.

To further probe gold-binding characteristics and explore the effects of the viral protein coat conformational change on mineralization, gold synthesis was completed with both spheroidal and filamentous M13 templates. Gold-binding templates were incubated in 250 μM $HAuCl_4$ with a pH near 6.7 for 1 hour. Despite the partial loss of helicity and reduced intermolecular π-π interaction associated with transformation, the s-forms remained stable at these slightly acidic conditions. $NaBH_4$ was then added step-wise 4 times, ultimately achieving a concentration of 62.5 μM. Representative synthesis products are shown for each step-wise

addition in Fig. 6. At the lowest $NaBH_4$ concentration, 4.2 μM, only gold ions (no nanoparticles) were observed bound to the spheroidal viral template. With subsequent $NaBH_4$ additions, 9.4 to 31.3 μM, the progressive reduction of gold ions produced several discrete nanoparticles which then grew in size. Spheroid-templated gold synthesis products stained with uranyl acetate confirmed particle clusters were associated with viral proteins (Fig. S12). At the highest $NaBH_4$ concentration, 62.5 μM, fused nanostructures with an average size of 86 ± 27 nm were produced on the template. While nanoparticles formed at lower $NaBH_4$ concentrations were relatively isotropic, as gold reduction advanced with step-wise $NaBH_4$ additions, highly anisotropic spike-like features also developed resulting in a range of morphologies (Fig. S13) and wide size distribution (Fig. S14).

To better elucidate the effect of the gold-binding spheroid on the formation of the spike-like structures, gold synthesis was performed without a viral template (Fig. S15) and in the presence of wild-type spheroids (Fig. S16) using a $NaBH_4$ concentration of 62.5 μM. Neither condition resulted in protruding, highly anisotropic features. Without a viral template, the average size of the synthesis products was only 10.2 ± 3.9 nm, while little to no nanoparticle growth was observed on the wild-type spheroids.

As shown in Fig. 6, like the spheroids, at the lowest $NaBH_4$ concentration, the filaments only showed evidence of gold ion binding and no nanoparticle growth. The step-wise reduction of gold ions yielded distinct gold nanoparticles which enlarged with each $NaBH_4$ addition eventually fusing with neighboring nanoparticles in some locations to form either (1) low aspect ratio ensembles with an average size of 38.2 ± 13.1 nm or (2) high aspect ratio chains with an average length and width of 71.1 ± 26.9 nm and 23.6 ± 6.1 nm, respectively. In contrast to the spheroid-templated nanostructures, prior to coalescence, the filament-templated nanoparticles remained fairly isotropic in structure with an average size of 5.8 ± 1.2 nm at 9.4 μM $NaBH_4$. Although the same gold synthesis conditions were used for both the M13 gold-binding spheroids and filaments, very different morphologies were produced.

The UV-Vis absorbance spectra of the highest $NaBH_4$ concentration synthesis products were measured and are shown in Fig. 7. Localized surface plasmon resonance (LSPR) was observed for both viral-templated materials. Among other parameters, LSPR absorption characteristics are controlled by nanoparticle size, shape, environment, and particle-particle

optical coupling. The optical absorbance of the spheroid-templated gold produced a broad, feature ranging from 500 nm to 900 nm with a maximum absorbance near 700 nm. This optical signature was consistent with the broad size distribution of the templated nanocrystalline, spiky gold nanostructures 86 ± 27 nm in size.[72–75] In contrast, filament-templated gold displayed an asymmetric, but well-defined absorbance peak centered at 556 nm with a long wavelength tail extending beyond 900 nm. Such optical behavior was attributed to the combination of gold nanoparticle ensembles and chains synthesized on the filament and was in agreement with previous reports.[76–80] The dissimilar spectra of the two templates was a direct consequence of the disparate morphologies of the spheroid- and filament-templated synthesis products.

Gold ion uptake, one potential source of the observed morphology difference between gold templated on spheroidal and filamentous templates, was investigated using ICP-MS. The equilibrium adsorption concentration plotted against gold ion concentration for both template geometries is shown in Fig. 8, along with corresponding Langmuir isotherm curve. Langmuir fit parameters, q_{max} and a, are found in Table 1. Maximum gold ion adsorption capacities of 2.7 x 10^{-5} mol/mg and 4.3 x 10^{-5} mol/mg were calculated for filaments and spheroids, respectively. The gold ion uptake for the spheroids was 1.6 times more than for the filaments, indicating a higher apparent affinity for gold. Assuming an equivalent number of gold-binding peptides were displayed on both M13 geometries, the peptide surface density was estimated to be 1.8 times larger for spheroids than filaments. This significant difference in gold-binding peptide areal density was likely responsible for the increased avidity and the ion adsorption capacity of the s-form. In addition, it may have had an important effect on nanostructure shape and size. The impact of increased localized peptide density caused by small peptide aggregates or clusters has been reported for PbSe[81] and Cu[82] nanoparticles synthesized on peptide nanotubes. In the former, peptide aggregation converted nanoparticle shape from cubes to rods. In the latter, peptide aggregation controlled Cu nanoparticle diameter and polydispersity. Furthermore, long range peptide packing density has also demonstrated influence over morphology. Peptide-templated gold nanoparticles synthesized at the air-water interface of a Langmuir trough showed morphologies ranging from triangle plates to star-like structure depending on peptide packing density.[83] In the present studies, increased gold ion uptake due to greater peptide surface density associated with the spheroidal templates is believed to have contributed to increased nanoparticle density and the formation of spike-like features.

4. Conclusions

In conclusion, we have studied the chloroform-triggered transformation of a gold-binding M13 bacteriophage and the templating properties of the resulting spheroids. The clone, with 100% display of an 8-mer gold-binding peptide on the pVIII major coat protein, was gradually converted from filaments to spheroids while monitoring protein ellipticity and viral geometry. Curiously, using the same procedure, somewhat larger and comparatively more spheroids were produced from the gold-binding phage than the wild-type phage. A change in pVIII protein-protein interactions within the viral coat caused by the peptide insert could be the source of size and conversion efficiency differences. More studies are necessary to better understand this phenomenon and possibly allow for spheroid size tunability. M13 spheroids were found to retain affinity for gold, demonstrating the ability to bind pre-formed colloidal gold nanoparticles as well as to direct gold synthesis. It was noted that the morphology of the synthesized gold nanostructures was dependent on the template geometry. Gold-binding M13 filaments yielded a mixture of isolated gold particle ensembles and chains composed of relatively isotropic nanoparticles while M13 spheroids produced nanostructures with anisotropic, spike-shaped features. The gold ion adsorption of spheroids was determined to be greater than that of filaments. We believe that this disparity contributed to the observed template-dependent gold morphological differences. The lower surface area of the spheroids likely increased surface packing of gold-binding peptides and lead to enhanced gold avidity. Further investigation is needed to better understand the density and organization of gold-binding peptides on the surface of the spheroid. Nonetheless, it is interesting to consider the potential of this scaffold to control gold morphology by modifying peptide surface density through genetic display or chemical conjugation. Furthermore, the promise and utility of the spheroidal template could be extended to other inorganic material systems via simple substitution of the displayed peptide.

Conflict of Interest

There are no conflicts to declare.

Acknowledgements

This material is based upon research supported by, or in part by, the U. S. Office of Naval Research under award number N00014-14-1-0799, the Regents' Faculty Fellowship, and the

UCR Collaborative Seed Grant Program. In addition, this study made use of the TEM FEI Tecnai12 in the Central Facility for Advanced Microscopy and Microanalysis (CFAMM) and the Jasco J-815 CD spectrophotometer in the Analytical Chemistry Instrumentation Facility (ACIF) at UC Riverside.

References

1 S. Sotiropoulou, Y. Sierra-Sastre, S. S. Mark and C. A. Batt, *Chem. Mater.*, 2008, **20**, 821–834.

2 F. Li and Q. Wang, *Small*, 2014, **10**, 230–245.

3 Z. Zhou, G. J. Bedwell, R. Li, N. Bao, P. E. Prevelige and A. Gupta, *Chem. Commun.*, 2015, **51**, 1062–1065.

4 A. Kadri, E. Maiß, N. Amsharov, A. M. Bittner, S. Balci, K. Kern, H. Jeske and C. Wege, *Virus Res.*, 2011, **157**, 35–46.

5 S. H. Yang, W.-J. Chung, S. McFarland and S.-W. Lee, *Chem. Rec.*, 2013, **13**, 43–59.

6 S. Balci, A. M. Bittner, K. Hahn, C. Scheu, M. Knez, A. Kadri, C. Wege, H. Jeske and K. Kern, *Electrochim. Acta*, 2006, **51**, 6251–6257.

7 D. Rothenstein, S. J. Facey, M. Ploss, P. Hans, M. Melcher, V. Srot, P. A. van Aken, B. Hauer and J. Bill, *Bioinspired Biomim. Nanobiomaterials*, 2013, **2**, 173–185.

8 Y. Li, B. Cao, M. Yang, Y. Zhu, J. Suh and C. Mao, *ACS Appl. Mater. Interfaces*, 2016, **8**, 30714–30721.

9 C. E. Flynn, S. W. Lee, B. R. Peelle and A. M. Belcher, *Acta Mater.*, 2003, **51**, 5867–5880.

10 K. M. Bromley, A. J. Patil, A. W. Perriman, G. Stubbs and S. Mann, *J. Mater. Chem.*, 2008, **18**, 4796–4801.

11 C. Jolley, M. Klem, R. Harrington, J. Parise and T. Douglas, *Nanoscale*, 2011, **3**, 1004–1007.

12 A. A. A. Aljabali, J. E. Barclay, G. P. Lomonossoff and D. J. Evans, *Nanoscale*, 2010, **2**, 2596–2600.

13 A. S. Blum, C. M. Soto, C. D. Wilson, J. D. Cole, M. Kim, B. Gnade, A. Chatterji, W. F. Ochoa, T. Lin, J. E. Johnson and B. R. Ratna, *Nano Lett.*, 2004, **4**, 867–870.

14 K. T. Nam, D.-W. Kim, P. J. Yoo, C.-Y. Chiang, N. Meethong, P. T. Hammond, Y.-M. Chiang and A. M. Belcher, *Science*, 2006, **312**, 885–888.

15 E. Royston, A. Ghosh, P. Kofinas, M. T. Harris and J. N. Culver, *Langmuir*, 2008, **24**, 906–912.

16 M. Gnerlich, E. Pomerantseva, K. Gregorczyk, D. Ketchum, G. Rubloff and R. Ghodssi, *J. Micromechanics Microengineering*, 2013, **23**, 114014.

17 C. H. Moon, M. Zhang, N. V Myung and E. D. Haberer, *Nanotechnology*, 2014, **25**, 135205.

18 L. Chen, Y. Wu, Y. Lin and Q. Wang, *Chem. Commun.*, 2015, **51**, 10190–10193.

19 B. Schwarz and T. Douglas, *Wiley Interdiscip. Rev. Nanomedicine Nanobiotechnology*, 2015, **7**, 722–735.

20 S. L. Capehart, M. P. Coyle, J. E. Glasgow and M. B. Francis, *J. Am. Chem. Soc.*, 2013, **135**, 3011–3016.

21 P.-Y. Chen, R. Ladewski, R. Miller, X. Dang, J. Qi, F. Liau, A. M. Belcher and P. T. Hammond, *J. Mater. Chem. A*, 2013, **1**, 2217–2224.

22 R. Zandi and D. Reguera, *Phys. Rev. E- Stat. Nonlinear, Soft Matter Phys.*, 2005, **72**, 021917.

23 J. Atabekov, N. Nikitin, M. Arkhipenko, S. Chirkov and O. Karpova, *J. Gen. Virol.*, 2011, **92**, 453–456.

24 M. A. Bruckman, S. Hern, K. Jiang, C. A. Flask, X. Yu and N. F. Steinmetz, *J. Mater. Chem. B. Mater. Biol. Med.*, 2013, **1**, 1482–1490.

25 N. Nikitin, A. Ksenofontov, E. Trifonova, M. Arkhipenko, E. Petrova, O. Kondakova, M. Kirpichnikov, J. Atabekov, E. Dobrov and O. Karpova, *FEBS Lett.*, 2016, **590**, 1543–1551.

26 M. A. Bruckman, L. N. Randolph, A. VanMeter, S. Hern, A. J. Shoffstall, R. E. Taurog and N. F. Steinmetz, *Virology*, 2014, **449**, 163–173.

27 M. A. Bruckman, A. VanMeter and N. F. Steinmetz, *ACS Biomater. Sci. Eng.*, 2015, **1**, 13–18.

28 C. F. Barbas, D. R. Burton, J. K. Scott and G. J. Silverman, *Phage Display: A Laboratory Manual*, CSHL Press, 2004.

29 M. B. Dickerson, K. H. Sandhage and R. R. Naik, *Chem. Rev.*, 2008, **108**, 4935–4978.

30 C. Tamerler, D. Khatayevich, M. Gungormus, T. Kacar, E. E. Oren, M. Hnilova and M. Sarikaya, *Biopolymers*, 2010, **94**, 78–94.

31 C. Mao, D. J. Solis, B. D. Reiss, S. T. Kottmann, R. Y. Sweeney, A. Hayhurst, G. Georgiou, B. Iverson and A. M. Belcher, *Science*, 2004, **303**, 213–217.

32 S. W. Lee, C. Mao, C. E. Flynn and A. M. Belcher, *Science*, 2002, **296**, 892–895.

33 C. E. Flynn, C. Mao, A. Hayhurst, J. L. Williams, G. Georgiou, B. Iverson and A. M. Belcher, *J. Mater. Chem.*, 2003, **13**, 2414–2421.

34 R. A. Blaik, E. Lan, Y. Huang and B. Dunn, *ACS Nano*, 2016, **10**, 324–332.

35 H. E. Lee, H. K. Lee, H. Chang, H. Y. Ahn, N. Erdene, H. Y. Lee, Y. S. Lee, D. H. Jeong, J. Chung and K. T. Nam, *Small*, 2014, **10**, 3007–3011.

36 L. I. Vera-Robles, G. Van Tran Nhieu, C. Laberty-Robert, J. Livage and C. Sanchez, *Adv. Eng. Mater.*, 2013, **15**, 954–961.

37 D. Montalvan-Sorrosa, J. L. González-Solis, J. Mas-Oliva and R. Castillo, *RSC Adv.*, 2014, **4**, 57329–57336.

38 Y. Huang, C. Y. Chiang, S. K. Lee, Y. Gao, E. L. Hu, J. De Yoreo and A. M. Belcher, *Nano Lett.*, 2005, **5**, 1429–1434.

39 N. Korkmaz, *Colloids Surfaces B Biointerfaces*, 2013, **112**, 219–228.

40 J. Griffith, M. Manning and K. Dunn, *Cell*, 1981, **23**, 747–753.

41 M. Manning, S. Chrysogelos and J. Griffith, *J. Virol.*, 1981, **40**, 912–919.

42 A. K. Dunker, L. D. Ensign, G. E. Arnold and L. M. Roberts, *FEBS Lett.*, 1991, **292**, 271–274.

43 L. M. Roberts and A. K. Dunker, *Biochemistry*, 1993, **32**, 10479–10488.

44 D. Stopar, R. B. Spruijt, C. J. A. M. Wolfs and M. A. Hemminga, *Biochemistry*, 1998, **37**, 10181–10187.

45 V. a Petrenko and G. P. Smith, *Protein Eng.*, 2000, **13**, 589–592.

46 E. V. Olsen, J. C. Sykora, I. B. Sorokulova, I.-H. Chen, W. C. Neely, J. M. Barbaree, V. A. Petrenko and V. J. Vodyanoy, *ECS Trans.*, 2007, **2**, 9–25.

47 B. Cao, H. Xu and C. Mao, *Microsc. Res. Tech.*, 2011, **74**, 627–635.

48 J. S. Lim, S. M. Kim, S. Y. Lee, E. A. Stach, J. N. Culver and M. T. Harris, *J. Colloid Interface Sci.*, 2010, **342**, 455–461.

49 Z. Reddad, C. Gerente, Y. Andres and P. Le Cloirec, *Environ. Sci. Technol.*, 2002, **36**, 2067–2073.

50 G. Limousin, J. P. Gaudet, L. Charlet, S. Szenknect, V. Barthès and M. Krimissa, *Appl. Geochemistry*, 2007, 22, 249–275.

51 J. Z. Porterfield and A. Zlotnick, *Virology*, 2010, **407**, 281–288.

52 H. M. Berman, *Nucleic Acids Res.*, 2000, **28**, 235–242.

53 D. A. Marvin, *Int. J. Biol. Macromol.*, 1990, **12**, 125–138.

54 F. M. Marassi and S. J. Opella, *Protein Sci.*, 2003, **12**, 403–411.

55 M. A. Marti-Renom, B. Yerkovich and A. Sali, in *Current Protocols in Protein Science*, John Wiley & Sons, Inc., Hoboken, NJ, USA, 2002.

56 E. F. Pettersen, T. D. Goddard, C. C. Huang, G. S. Couch, D. M. Greenblatt, E. C. Meng and T. E. Ferrin, *J. Comput. Chem.*, 2004, **25**, 1605–1612.

57 D. A. Marvin, R. D. Hale, C. Nave and M. H. Citterich, *J. Mol. Biol.*, 1994, **235**, 260–286.

58 D. Marvin, *Curr. Opin. Struct. Biol.*, 1998, 8, 150–158.

59 D. Stopar, R. B. Spruijt, C. J. A. M. Wolfs and M. A. Hemminga, *Biochim. Biophys. Acta - Biomembr.*, 2003, 1611, 5–15.

60 R. B. Spruijt, C. J. A. M. Wolfs and M. A. Hemminga, *Biochemistry*, 2004, **43**, 13972–13980.

61 K. A. Williams and C. M. Deber, *Biochemistry*, 1996, **35**, 10472–10483.

62 G. E. Arnold, L. a Day and a K. Dunker, *Biochemistry*, 1992, **31**, 7948–7956.

63 G. J. Hunter, D. H. Rowitch and R. N. Perham, *Nature*, 1987, **327**, 252–254.

64 H. Endemann and P. Model, *J. Mol. Biol.*, 1995, **250**, 496–506.

65 N. J. Greenfield, *Nat. Protoc.*, 2006, **1**, 2876–2890.

66 M. Manning, M. Moore, L. Spremulli and J. Griffith, *Biochem. Biophys. Res. Commun.*, 1983, **112**, 349–355.

67 C. T. K. Yuen, A. R. Davidson and C. M. Deber, *Biochemistry*, 2000, **39**, 16155–16162.

68 D. Stopar, R. B. Spruijt, C. J. A. M. Wolfs and M. A. Hemminga, *Biochim. Biophys. Acta - Protein Struct. Mol. Enzymol.*, 2002, **1594**, 54–63.

69 J. Beaudoin, T. J. Henry and D. Pratt, *J. Virol.*, 1974, **13**, 470–477.

70 L. Specthrie, E. Bullitt, K. Horiuchi, P. Model, M. Russel and L. Makowski, *J. Mol. Biol.*, 1992, **228**, 720–724.

71 S. Sattar, N. J. Bennett, W. X. Wen, J. M. Guthrie, L. F. Blackwell, J. F. Conway and J. Rakonjac, *Front. Microbiol.*, 2015, **6**, 316.

72 B. G. Prevo, S. A. Esakoff, A. Mikhailovsky and J. A. Zasadzinski, *Small*, 2008, **4**, 1183–1195.

73 M. R. Rasch, K. V. Sokolov and B. A. Korgel, *Langmuir*, 2009, **25**, 11777–11785.

74 E. Hao, S. Y. Li, R. C. Bailey, S. L. Zou, G. C. Schatz and J. T. Hupp, *J. Phys. Chem. B*, 2004, **108**, 1224–1229.

75 S. N. Abdollahi, M. Naderi and G. Amoabediny, *Colloids Surfaces A Physicochem. Eng. Asp.*, 2013, **436**, 1069–1075.

76 A. Albanese and W. C. W. Chan, *ACS Nano*, 2011, **5**, 5478–5489.

77 Y. Yang, S. Matsubara, M. Nogami, J. Shi and W. Huang, *Nanotechnology*, 2006, **17**, 2821–2827.

78 N. G. Khlebtsov, A. G. Melnikov, L. A. Dykman and V. A. Bogatyrev, in *Photopolarimetry in Remote Sensing*, eds. G. Videen, Y. Yatskiv and M. Mishchenko, Springer Netherlands, Dordrecht, 2005, pp. 265–308.

79 S. J. Barrow, A. M. Funston, D. E. Gómez, T. J. Davis and P. Mulvaney, *Nano Lett.*, 2011, **11**, 4180–4187.

80 A. A. Lazarides and G. C. Schatz, *J. Phys. Chem. B*, 2000, **104**, 460–467.

81 M. Shi, W. Su and H. Matsui, *Nanoscale*, 2010, **2**, 2373–2376.

82 I. A. Banerjee, L. Yu and H. Matsui, *Proc. Natl. Acad. Sci.*, 2003, **100**, 14678–14682.

83 L. Leon, W. Su, H. Matsui and R. Tu, *Soft Matter*, 2011, **7**, 10285–10290.

Figures

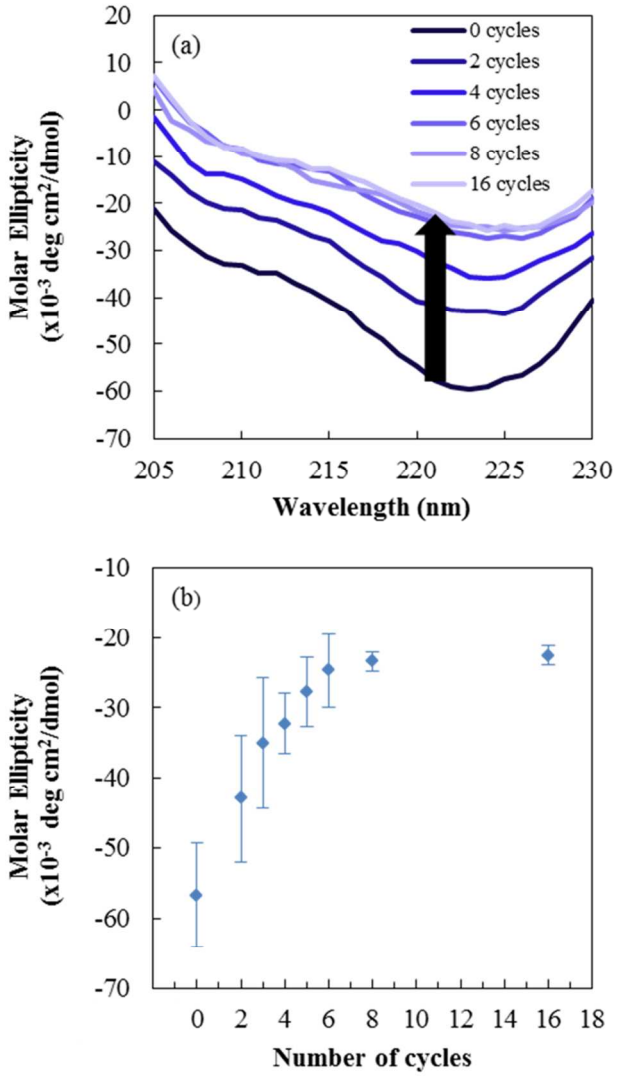

Fig. 1. (a) Circular dichroism (CD) spectra and (b) 222 nm molar ellipticity values for gold-binding M13 bacteriophage measured as a function of cycle number. The black arrow in (a) indicates increasing cycle number.

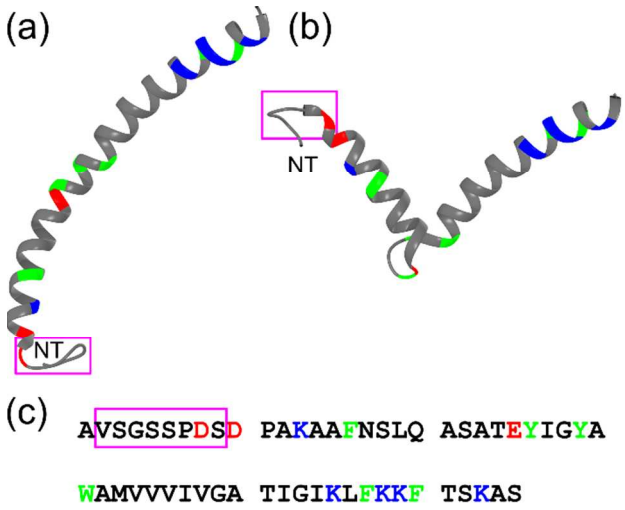

Fig. 2. Homology models of M13 with a gold-binding peptide (VSGSSPDS) at the N-termini, NT, (a) pre- and (b) post-chloroform treatment. Both structures share a common sequence, as illustrated in (c). Residues are colored green, red, and blue to identify aromatic, negative, and positive residues, respectively. The gold-binding peptide is boxed in magenta.

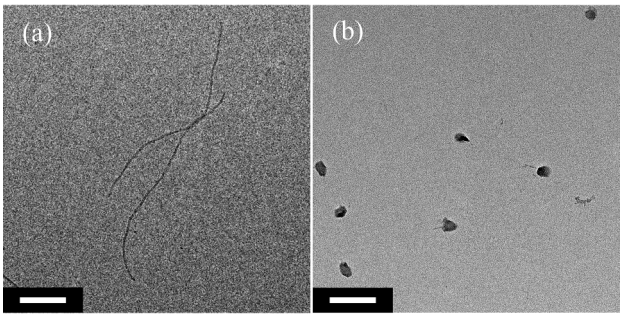

Fig. 3. Transmission electron microscopy (TEM) images of gold-binding M13 bacteriophage (a) pre- and (b) post-chloroform treatment (5 cycles). Samples were stained with 0.5% uranyl acetate; scale bar: 200 nm.

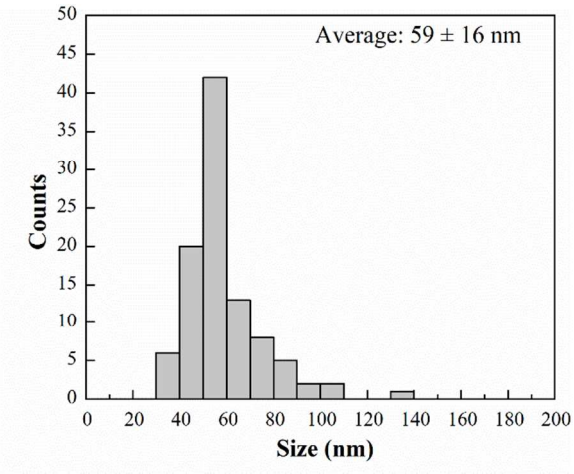

Fig. 4. A histogram of the spheroid size distribution following 5 chloroform treatment cycles (N = 100).

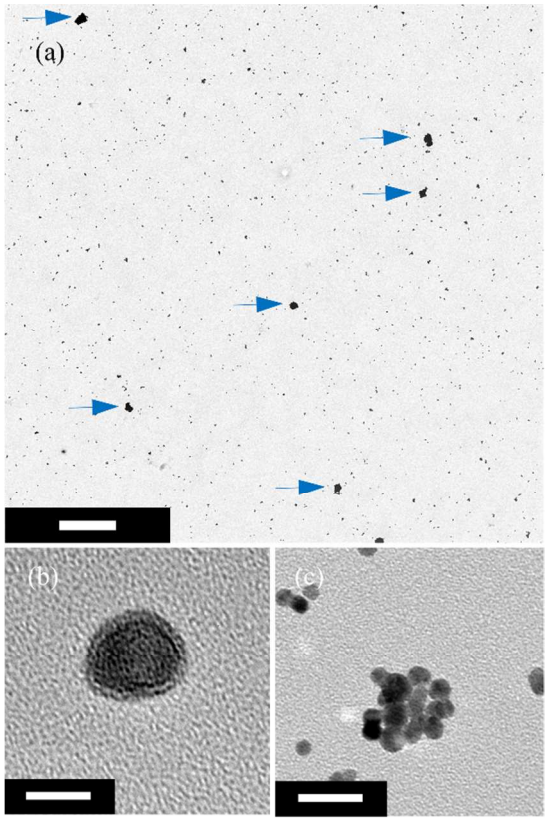

Fig. 5. (a) TEM image of several spheroid-templated gold colloid clusters with excess unbound colloid; scale bar: 500 nm. Templated nanostructures are indicated by arrows. An individual gold-binding spheroid (b) without and (c) with 5 nm colloidal gold nanoparticles arranged on the surface to form a cluster; scale bar: 20 nm.

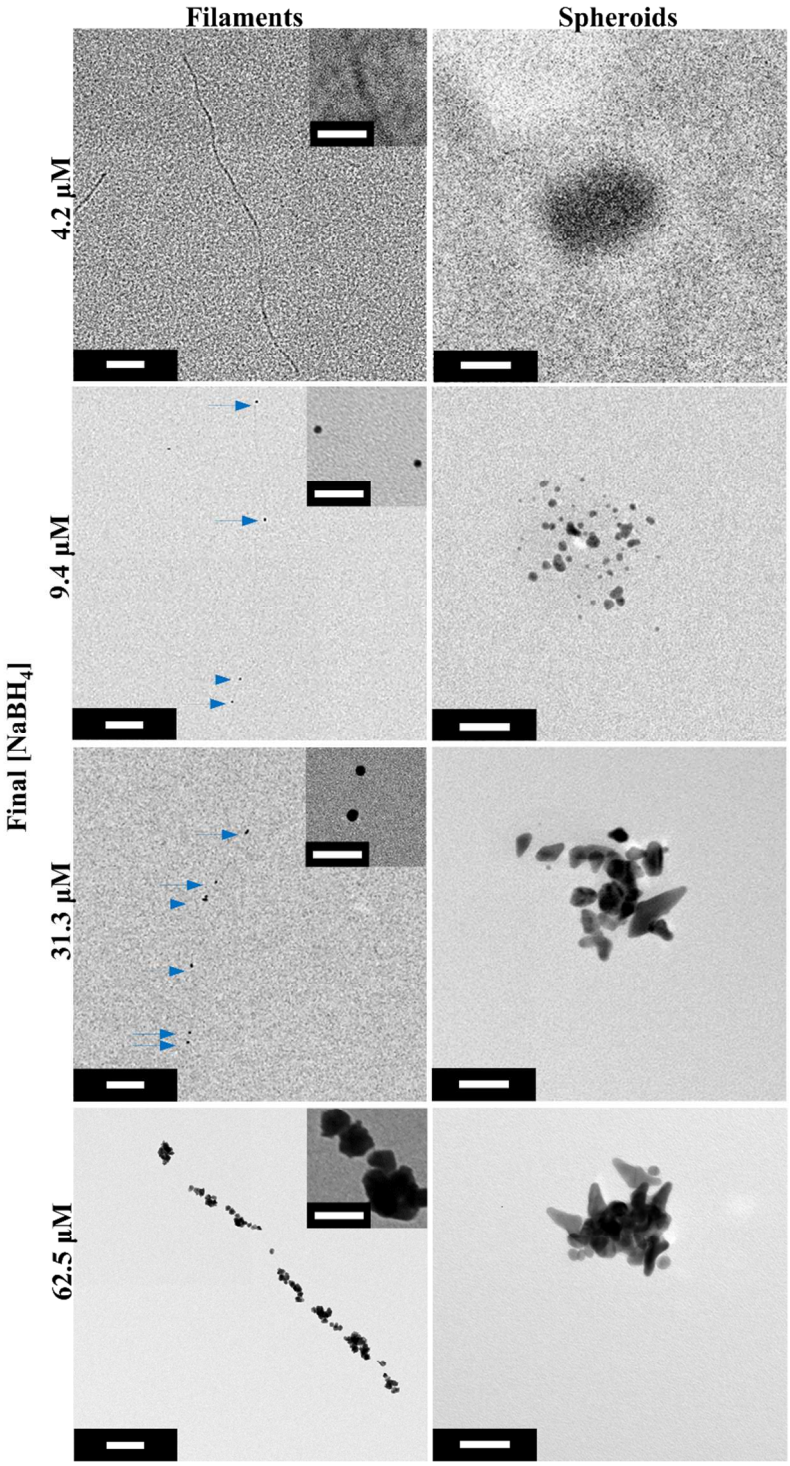

Fig. 6. Comparison of gold nanomaterials synthesized on filamentous (scale bar: 100 nm) and spheroidal templates (scale bar: 25 nm) following the addition of $NaBH_4$ at different concentrations. High magnification images of filament-templated materials are shown within the insets (scale bar: 25 nm).

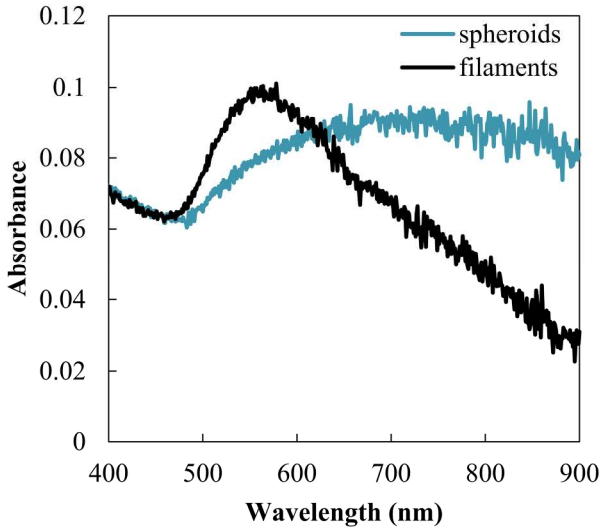

Fig. 7. UV-Vis absorbance spectra of gold synthesis products on filamentous and spheroidal templates using a final $NaBH_4$ concentration of 62.5 μM.

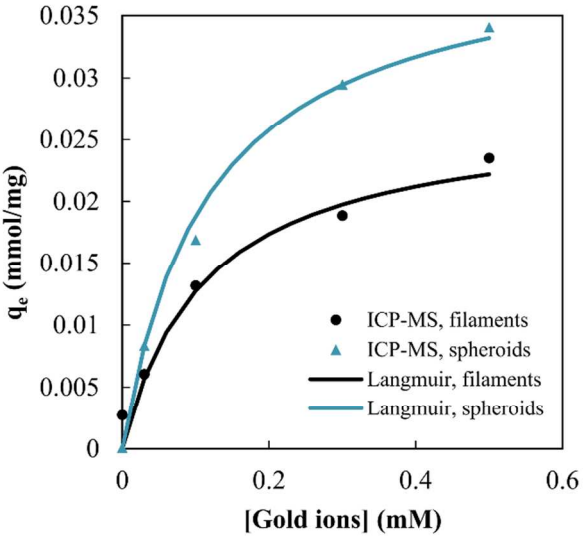

Fig. 8. Adsorption isotherm of gold ions onto the M13 spheroids and filaments.

Table 1. Equilibrium Coefficients of Langmuir Adsorption Isotherm

Template	q_{max} (mol mg^{-1})	a (L mol^{-1})	R^2
Filament	2.7×10^{-5}	8782	0.994
Spheroid	4.3×10^{-5}	8509	0.996

Table of Contents Entry

for

Manuscript ID: NR-ART-04-2018-003229.R1

Title: M13 bacteriophage spheroids as scaffolds for directed synthesis of spiky gold nanostructures

Authors: Tam-Triet Ngo-Duc, Joshua M. Plank, Gongde Chen, Reed E. S. Harrison, Dimitrios Morikis, Haizhou Liu, Elaine D. Haberer

Text (20 words max):

A gold-binding filamentous virus was converted to its spheroidal form and investigated as a versatile template of nanostructure formation.

Graphic: